

Master Thesis

**Study on effect of radiative loss on waves in
solar chromosphere**

Wang Yikang

**Department of Earth and Planetary Science
Graduate School of Science, The University of Tokyo**

September 4, 2017

Abstract

The chromospheric and coronal heating problem that why the plasma in the chromosphere and the corona could maintain a high temperature is still unclear. Wave heating theory is one of the candidates to solve this problem. It is suggested that Alfvén wave generated by the transverse motion at the photosphere is capable of transporting enough energy to the corona. During these waves propagating in the chromosphere, they undergo mode conversion and generate longitudinal compressible waves that are easily steepening into shocks in the stratified atmosphere structure. These shocks may contribute to chromospheric heating and spicule launching. However, in previous studies, radiative loss, which is the dominant energy loss term in the chromosphere, is usually ignored or crudely treated due to its difficulty, which makes them unable to explain chromospheric heating at the same time. In our study, based on the previous Alfvén wave driven model, we apply an advanced treatment of radiative loss. We find that the spatial distribution of the time averaged radiative loss profile in the middle and higher chromosphere in our simulation is consistent with that derived from the observation. Our study shows that Alfvén wave driven model has the potential to explain chromospheric heating and spicule launching at the same time, as well as transporting enough energy to the corona.

Contents

Abstract	i
1 Introduction	1
1.1 General introduction	1
1.2 Radiation in the chromosphere	4
1.3 Observation of waves in the chromosphere	6
1.4 Theoretical models of waves in the chromosphere	9
1.5 Remained Problems and Purpose of the Study	12
2 Method	15
2.1 Geometry	15
2.2 Basic equations	15
2.3 Initial conditions	21
2.4 Boundary conditions and numerical scheme	22
3 Results and analysis	25
3.1 Introduction	25
3.2 Role of radiative loss	25
3.3 Relation between initial wave amplitude and energy flux in the corona	30
3.4 Effect of flux tube expanding	30
3.5 Effect of input wave spectrum and the photosphere magnetic field	34

4 Discussion	39
4.1 Spatial distribution of radiative loss	39
4.2 Estimation of the expanding factor	40
4.3 Comparison with previous researches	41
5 Summary and Future Prospects	45
Acknowledgments	47
References	49

Chapter 1

Introduction

1.1 General introduction

Solar atmosphere is generally considered to be divided into three layers. Starting from the bottom, they are the photosphere, the chromosphere and the corona. The bottom of the photosphere is defined as the optical depth of 500 nm-wavelength-radiation equals to unity. Figure 1.1 gives a preview of different layers of the solar atmosphere. VAL model (Figure 1.2, Vernazza et al., 1981) is a series of classical 1D solar atmosphere models that give the distribution of pressure, density, radiative loss, etc., as a function of height. The most frequently used one, which is called VALC, describes an averaged atmosphere above solar quiet regions. We will mention this model later in the following contents of this thesis.

According to VAL model, the deepest photosphere is of the highest density which is usually observed by continuum radiation of visible light. The density and gas pressure decreases gradually with height. Between the chromosphere and the corona lies a thin layer called the transition region with a sudden increase of temperature from around 10^4 K to 10^6 K. Density also decreases accordingly. The atmosphere above the transition region is called the corona characterized by low density and high temperature. Distribution of temperature in this model is shown in Figure 1.2. It is still not clear why the corona

could maintain such a high temperature. This problem is called coronal heating problem, which is one of the biggest mystery in solar physics. It is estimated that the typical value of required energy flux for coronal heating is $3 \times 10^5 \text{ erg cm}^{-2}\text{s}^{-1}$ (Withbroe & Noyes, 1977).

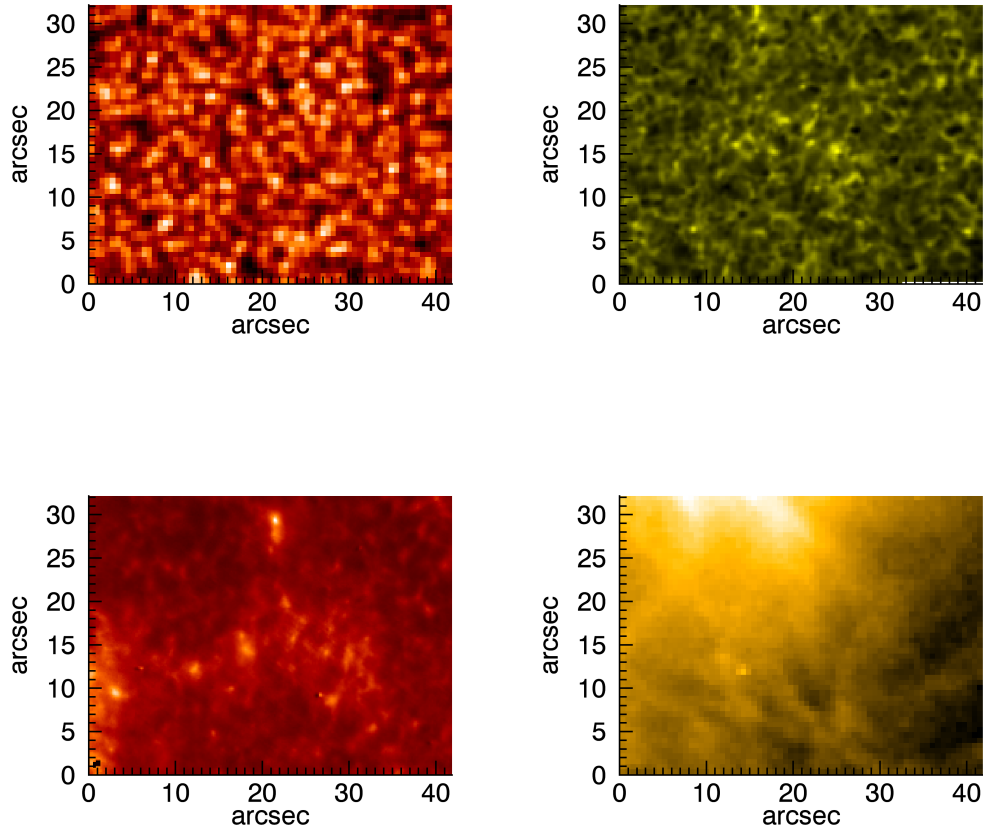


Figure 1.1: Observation of the same quiet sun region near disk center on Sep 25, 2013 from different wavelength. Upper-left: White light continuum observation of the photosphere observed by Helioseismic and Magnetic Imager (HMI; Scherrer et al., 2012). The photosphere is characterized by convection motion which has a typical scale of 1 Mm. Upper-right: Ca II H line observation of the lower chromosphere by SOT. Lower-left: Mg h line observation of the higher chromosphere and the transition region by IRIS. Bright strip in upper-right and this panel indicates the network region. Lower-right: EUV Observation of high temperature plasma in the corona by AIA. Note that strong radiation from the top of this panel comes from a nearby active region.

The medium chromosphere, sandwiched between dense photosphere and hot corona,

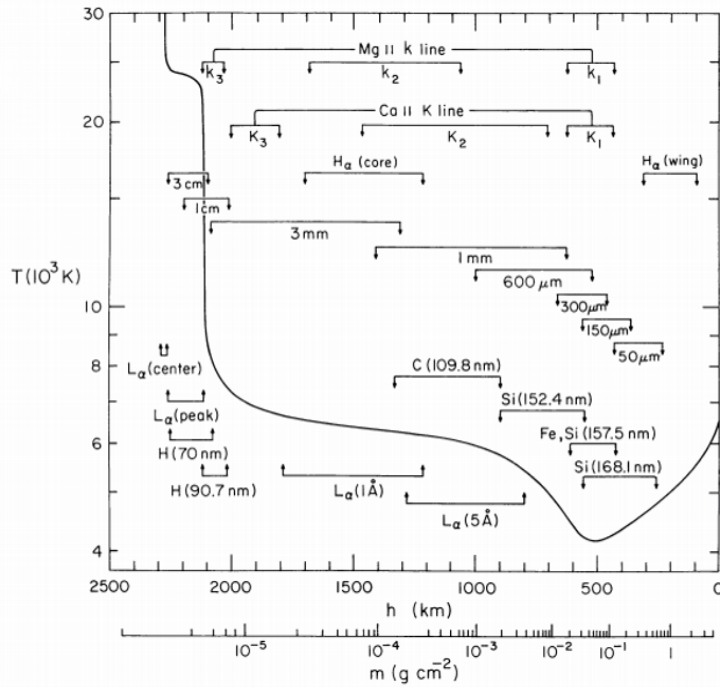


Figure 1.2: Temperature distribution of solar atmosphere derived from EUV spectra (Verzazza et al., 1981). Short bars indicate the approximate formation height of corresponding radiation

plays a crucial role in energy and mass transportation. In addition, a high temperature is also maintained in the chromosphere. Although the temperature of the chromosphere is low compared with that of the corona, the chromosphere is much denser than the corona and consequently requires more energy to maintain this temperature distribution. We usually imagine that the temperature will decrease as moving away from the energy source, which is inconsistent with the temperature distribution described in Figure 1.2. This abnormal temperature distribution can not be explained by a pure thermodynamic process. It is believed that convection motion below atmosphere contains plenty of energy for heating the upper atmosphere. Besides, we have also learned that dominant energy loss term in the chromosphere is radiative loss (Withbroe & Noyes, 1977). Then the problem in the chromosphere becomes how to absorb enough energy from convection motions to compensate radiative loss and how to transport enough energy to the corona above it at the same time. One candidate for this energy transporting process is wave, which is the main subject of this thesis and is described in detail below. Observations of waves in

the chromosphere have been already done by previous studies (e.g. Tian et al., 2014a; De Pontieu et al., 2007b; Kanoh et al., 2016). It is also noticed that small scale magnetic reconnection could also be an important energy source for chromospheric and coronal heating while lack of direct observational evidence.

1.2 Radiation in the chromosphere

Radiative loss is the most significant source of energy loss in the chromosphere (Withbroe & Noyes, 1977). In a rough estimation by Anderson & Athay (1989), energy dissipated by sound waves is consistent with energy loss by radiation in terms of both magnitude and spatial distribution, by a factor difference that dissipated energy is around 2.6 larger than energy loss by radiation.

To solve the radiation problem, which means to obtain the intensity as a function of position and frequency at a certain time, as a standard method, one needs to solve the radiative transfer equation below

$$\frac{dI}{ds} = j - a \quad (1.1)$$

where I , j , and a represent intensity, emission and absorption, respectively. Strictly speaking they are all function of position, angle, frequency, and local physical parameters. s is the distance along the direction of the light. In addition, j and a are also functions of I . For simplicity, we assume a plane parallel atmosphere that stratified in a direction \mathbf{k} (all the physical parameters are the same in the plane perpendicular to \mathbf{k}). Energy flux of radiation F_r could be calculated as

$$F_r = \frac{1}{4\pi} \int_{4\pi} I \cos \theta d\Omega \quad (1.2)$$

where θ is the angle of between a specific direction and the direction \mathbf{k} . Ω is solid angle.

Radiative loss L is given by divergence of radiative energy flux F_r

$$L = -\frac{\partial F_r}{\partial s} \quad (1.3)$$

where s is the spatial coordinate on the line of propagation.

From microscopic point of view, the energy is lost by collisional excitation which consumed the kinetic energy of electrons, followed by stimulated de-excitation or spontaneous de-excitation that release photons which escape away. The pure effect of this process is that the internal energy is converted to radiative energy. A completed treatment of radiation requires solving radiative transfer equation 1.1. In the local thermodynamic equilibrium (LTE) assumption which is rather a good approximation for the photosphere, collision dominates over radiation in determining number density of electrons at each energy level. It is shown that in this case, $I_\nu = B_\nu(T)$, Where B_ν is Planck function for frequency ν . Under this approximation, I could be locally determined and radiative loss rate could also be easily calculated. Unfortunately, this is not the case for the chromosphere. In the chromosphere, density decrease drastically as height increases, as a result, the strength of collision decreases and become comparable to radiation. This situation is called the non local thermodynamic equilibrium (NLTE). Under this circumstance, equations of electron number density on different energy levels need to be solved. In addition, intensity can not be locally determined. This adds the difficulty in solving the intensity as well as extracting physical information from the observed intensity data.

In the VAL model (Vernazza et al., 1981), in order to derive values of different physical parameters as a function of height, a hydrostatic stratified atmosphere model is assumed. Considering NLTE radiative transfer calculation for more than 10 kinds of atoms and ions, adjusting temperature distribution by trial and error, they finally succeed in obtaining the semi-experiential temperature distribution that emergent EUV spectra could match observed spectra well. Radiative loss rate is also given from their calculation, Figure 1.3 shows the distribution of radiative loss rate. Effective components for radiative loss

in the chromosphere include H, Mg II and Ca II. Anderson & Athay (1989) point out that in middle and higher part of the chromosphere, radiative loss is characterized by a single number $4.5 \times 10^9 \text{ erg g}^{-1}\text{s}^{-1}$. However, real chromosphere is highly dynamic and radiative loss is far from a homogeneous single value. In addition, radiative hydrodynamic simulations show that radiative loss is especially effective at shock fronts (Carlsson & Leenaarts, 2012).

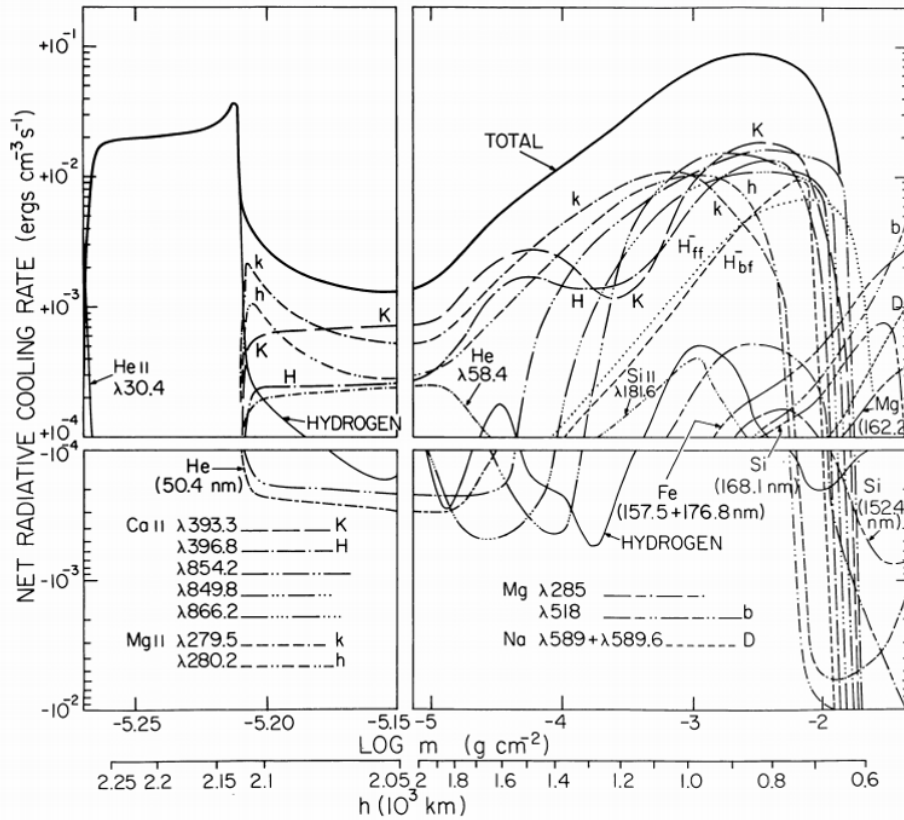


Figure 1.3: Distribution of radiative loss derived from EUV spectra. The most important components of radiative loss include Mg II h& k lines, Ca II H & K lines and Hydrogen. (Vernazza et al., 1981).

1.3 Observation of waves in the chromosphere

The chromosphere of the sun could mainly be observed by continuum of millimeter, UV and EUV bands, as well as spectral lines in infrared, visible, UV and EUV bands. where the UV and EUV continuum opacity is mainly dominated by carbon and silicon bound-

free transition. Observing solar chromosphere is not an easy task because signal-to-noise ratio of absorption lines core is low while longer exposure time will remove short period information (Jess et al., 2015). In addition, a number of characteristic lines are located out of the atmospheric window. Strong lines in the chromosphere include Ca II H&K line, $H\alpha$ line, Mg II h&k line and Lyman α line.

Currently, large telescopes for observing the chromosphere in operation include Solar Optical Telescope (SOT; Tsuneta et al., 2008) onboard Hinode (Kosugi et al., 2007) in Ca II band (Figure 1.4), Swedish Solar Telescope (SST; Scharmer et al., 2003) in $H\alpha$ band. New Vacuum Solar Telescope (NVST; Liu et al., 2014) in $H\alpha$ band, Interface Region Imaging Spectrograph (IRIS; De Pontieu et al., 2014) in Mg II h&k band, Atmospheric Imaging Assembly (AIA; Lemen et al., 2012) on board Solar Dynamics Observatory (SDO; Pesnell et al., 2012) 304Å band as well as Atacama Large Millimeter/submillimeter Array (ALMA; Shimojo et al., 2017) in millimeter observation. Direct diagnostic from these observations include Doppler velocity for line observations and temperature from ALMA observation.

SOT could provide observations with unprecedented spatial and temporal resolution in Ca II band (Figure 1.4). These observations reveal a highly dynamic picture of solar chromosphere. Ubiquitous needle-like structures, which are called spicules, are detected at the solar limb. Spicules could extend from few Mm to over 10 Mm in height (Tsiropoula et al., 2012) and are considered as evidence of ubiquitous Alfvénic wave which is responsible for coronal heating (De Pontieu et al., 2007b). Similar structures have also been detected in observations by IRIS (Tian et al., 2014b) which diagnose plasma of higher temperature. Spicules are considered to be divided into two types (De Pontieu et al., 2007a), the so-called type-I and type-II spicules, where type-I spicules are shorter and have a longer lifetime, which undergo ballistic motion, while type-II spicules behave more active and have a shorter life time. Type-II spicules usually disappear in Hinode SOT Ca II image after upward propagating phase. IRIS observation suggests that type-II spicules continue propagating after disappearing from SOT Ca II image and also show

a full ballistic motion as type-I spicules. Their disappearance in Ca II observation indicates that they could be heated to higher temperature during its upward propagating phase (Skogsrud et al., 2015). Disk counterparts of spicules are also identified as subset of quiet sun mottles, dynamic fibrils and rapid blueshifted excursions (RBEs) (De Pontieu et al., 2007a; Langangen et al., 2008)

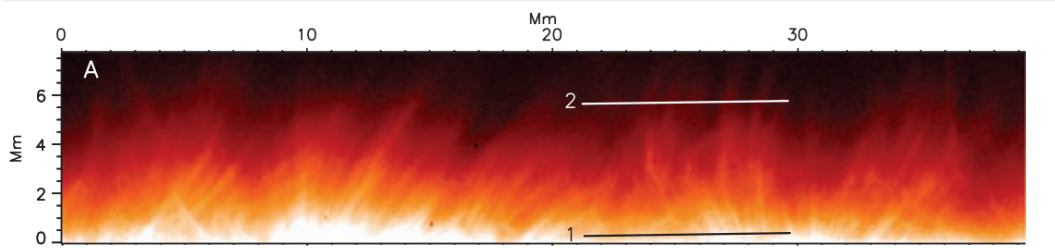


Figure 1.4: Observation by SOT Ca II band at the solar limb reveals the existence of ubiquitous needle-like structures which are called spicules (De Pontieu et al., 2007b).

Observations related to chromospheric heating problem usually concentrate on wave energy flux. Unfortunately, currently we can not obtain a definite conclusion of whether the acoustic wave is sufficient in supplying energy for radiative loss, neither can we give the opposite conclusion. Bello González et al. (2010) analyze observations by Imaging Magnetograph eXperiment (IMaX; Martínez Pillet et al., 2011) onboard Sunrise balloon-borne solar observatory of Fe I 525.02 nm line which forms around 200-300 km above the bottom of the photosphere. In their analysis, acoustic flux of around 6500 W m^{-2} is detected which is enough for supporting chromospheric radiative loss. On the other hand, Fossum & Carlsson (2005) use Transition Region and Coronal Explorer (TRACE) observation of 1700 \AA and 1600 \AA bands which sample around 360km and 430km above the bottom of the photosphere respectively. Their observation combining with simulations suggest that the acoustic flux is only 438 W m^{-2} which is far from supporting chromospheric radiative loss (e.g. 4300 W m^{-2} , Vernazza et al., 1981). Bello González et al. (2010) suggest that observed flux is significantly affected by spatial resolution. Sobotka et al. (2016) use Interferometric Bidimensional Spectrometer (IBIS Cavallini, 2006) observation of Ca II 854.2 nm line and show that radiative losses and deposited acoustic flux

are spatially correlated, which confirms the significance of acoustic wave in supporting radiative loss in the chromosphere. On the other hand, the contribution of acoustic energy flux to radiative losses is around 23% to 54%, which increases with activity, while still insufficient to balance the radiative loss.

For a comprehensive understanding of atmosphere heating problem, the significance of the chromosphere can never be overestimated. Hence, the chromosphere becomes one of the most important targets of the next generation solar observatories. Among them include Solar-C (Suematsu & Solar-C Working Group, 2016), European Solar Telescope (EST; Matthews et al., 2016), Daniel K. Inouye Solar Telescope (DKIST; Tritschler et al., 2015) and Chinese Giant Solar Telescope (CGST; Deng et al., 2012). Next generation solar telescopes are designed to have extraordinary unprecedented time and spatial resolution to catch fine structures and short-period dynamic processes as well as equipped with high sensitivity detectors for measuring full stokes profile for detecting weak magnetic field in the chromosphere.

1.4 Theoretical models of waves in the chromosphere

Observations with high time and spatial resolution have revealed that solar atmosphere is highly dynamic and full of fine structures, which bring huge challenge for establishing theoretical models.

Figure 1.5 from Wedemeyer-Böhm et al. (2009) shows recent models of lower quiet region atmosphere. Starting from the convection region below the atmosphere. Where plasma beta is high, convection motion of supergranulation transport the magnetic field lines to the boundary of convection cell and forms the enhanced magnetic field regions, which are called network regions. Motions at the lower boundary of the photosphere trigger different kinds of waves. As these waves propagating upwards, along with the violent change of background physical conditions, They undergo various changes in the chromosphere. Described under a MHD scheme, these effects include steepening of compressible

wave, mode coupling between Alfvén wave mode and magnetosonic wave mode near the equipartition layer and wave interaction and reflection at the transition region, etc. Looking back to the atmosphere heating problem, previous works conclude that shock heating could be the dominant heating mechanism in the chromosphere (Arber et al., 2016) that we may pay more attention to the wave driving and steepening process. Since we have already learned that a large amount of energy is stored in convection motion under the photosphere, the remaining problem is how to transport energy to the chromosphere and the corona by waves and how to dissipate the energy. In addition, as compressible waves are closely related to the origin of spicules (see the review paper by Sterling, 2000), these ubiquitous small jets could act as good indicator for studying wave propagation in the chromosphere.

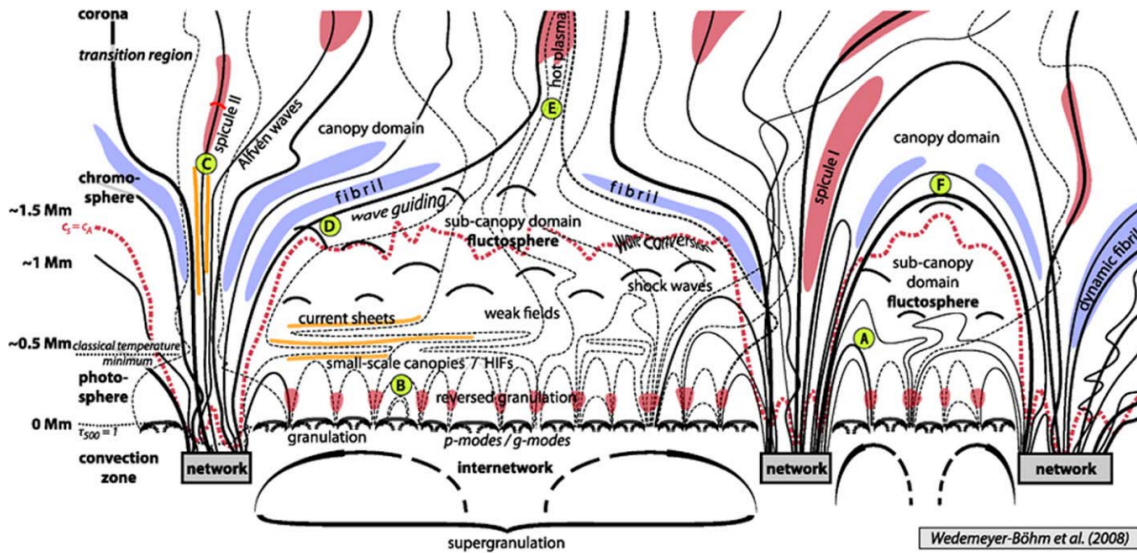


Figure 1.5: Schematic plot of recent model of structures in lower quiet sun atmosphere from Wedemeyer-Böhm et al. (2009). Solid black lines show magnetic field lines rooted in network region. Dashed black lines indicate magnetic field lines originated in internetwork region. Red dashed line represents equipartition layer. A-F stand for typical structures or behaviors of atmospheres. A: a magnetic field line connecting network and internetwork regions which indicates that there is no distinct boundary between network and internetwork region. B: weak magnetic field emerges in the form of small loops inside a granule cell. C: a type-II spicule. D-F all stand for wave-canopy interaction.

Numerical simulation is proved to be one of the powerful tools for approaching the

complicated physics in the chromosphere. Earlier stage researchers (e.g. Suematsu et al., 1982; Sterling et al., 1993) focus on the propagation of compressible waves which steepen into shocks as propagating upward. By applying hydrodynamic simulation. Spicules are found to be driven by shock interacting with the transition region and lifting the chromosphere matters upward. Recently, Guerreiro et al. (2013) consider the effect of detailed NLTE radiative loss in their simulation, when comparing with Sterling et al. (1993), they find that the height of spicule is obviously suppressed which suggests the importance of the effect of radiative cooling on waves in the chromosphere.

It becomes a milestone that Kudoh & Shibata (1999) investigate wave propagation in expanding flux tube under continuous input of Alfvén wave at the bottom. In their MHD simulation, transverse waves are imposed to mimic the convection motion at the bottom of the photosphere. They found that longitudinal motion is excited by the transverse waves near the photosphere through nonlinear coupling. Compressible longitudinal waves will steepen to shocks to lift the transition region and launch spicules by the similar process as Suematsu et al. (1982) and Sterling et al. (1993). On the other hand, incompressible Alfvén wave propagating into the corona may contribute to coronal heating. In their research, when applying a random transverse torque at the bottom which leads to an amplitude of the transverse wave of around 1 km/s, mean value of the energy flux in the corona is greater than $3 \times 10^5 \text{ erg cm}^{-2}\text{s}^{-1}$, which is the required energy for coronal heating. Brady & Arber (2016) perform 2.5D resistive MHD simulation, where waves are also initialized by transverse motion in the photosphere. From their simulation, calculated shock heating rate in the chromosphere are concluded to be consistent with chromospheric heating in terms of both magnitude and spatial distribution. In addition, rise of dense material is consistent with Type-I spicules in terms of raising velocity. However, their simulation does not treat radiative loss in detail.

With the assist of supercomputers, it is even possible to carry out 3D MHD simulations with simplification on radiative transfer. It is noticed that while 3D simulations are beneficial in interpreting chromospheric behaviors, even part of which can only be

explained in 3D geometry, for example, the driving mechanism of tall spicules (Iijima, 2016; Martínez-Sykora et al., 2017), the complex nature of the chromosphere itself may add the difficulties in diagnosing basic heating contribution (Jess et al., 2015).

1.5 Remained Problems and Purpose of the Study

We have briefly introduced the observational characteristics of the chromosphere and theoretical attempts in the chromospheric heating problem and spicule launching. We are closer and closer to the answer for atmosphere heating mystery while there are still many problems to be solved. From an observational perspective, it is believed that acoustic waves is important for chromospheric heating while there is not a clear conclusion whether the energy carried by the acoustic wave is enough or not for chromospheric heating. From theoretical perspective, MHD simulations succeed in explaining energy flux for coronal heating and type-I spicule launching by Alfvén wave model (Kudoh & Shibata, 1999). Since the important radiative loss effect is usually absent in previous researches, we do not have a comprehensive understanding on the effect of radiative loss in wave heating picture. Saying, we are not so confident about whether the Alfvén wave driven model still performs well after the participation of radiative loss. Though 3D MHD simulation (Iijima, 2016; Gudiksen et al., 2011) is a powerful tool in interpreting chromosphere dynamics, they require huge computational resources and their complicity may introduce difficulties when attempting to efficiently and accurately diagnose basal heating contributions (Jess et al., 2015).

The purpose of this study is to investigate the effect of radiative loss on waves in the chromosphere as well as give a trial on a relatively simple atmosphere model that could explain chromospheric heating, spicule launching as well as enough energy transportation to the corona simultaneously. For this purpose, we performed a series of one-dimensional MHD simulations by including an advanced radiative loss treatment (Carlsson & Leenaarts, 2012) into the Alfvén wave driven model (Kudoh & Shibata, 1999).

We are able to investigate the effect of radiative loss on wave propagation, spicule formation in detail and under different initial conditions. We will also check whether the Alfvén wave driven model works well with the participation of radiative loss, or in what condition does it work well.

Chapter 2

Method

2.1 Geometry

We consider an axisymmetric geometry setting of an expanding flux tube following previous researches (Hollweg et al., 1982; Kudoh & Shibata, 1999; Matsumoto & Shibata, 2010). This setting mimics the network region shown in Figure 2.1. The longitudinal section of the flux tube is schematically plotted in Figure 1.5 while the degree of expansion may vary in different cases that will be shown again case by case in the next section. The radius of the flux tube at the lower boundary is set to be 150 km which is approximately the length of pressure gradient height.

2.2 Basic equations

We solve 1.5D ideal compressible MHD equations on this expanding flux tube, following Matsumoto & Shibata (2010). 1.5D here refers to that we have one dimensional geometry setting while velocity has two components which are s direction and ϕ direction. s direction is the local direction of the field line, ϕ direction is the azimuthal direction. Basic equations are listed as follows. The meaning of each character is listed in Table 2.1 below

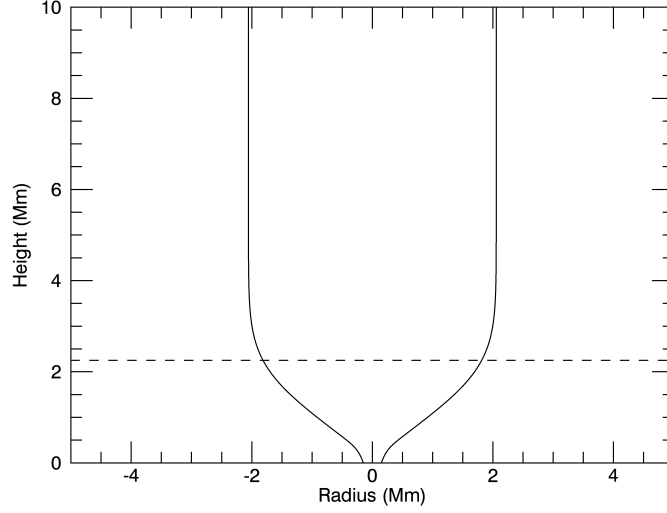


Figure 2.1: Schematic plot of the shape of the expanding flux tube. Dashed line shows the height of the transition region, which is 2.25 Mm in this study.

the equations.

$$\frac{\partial}{\partial t}(\rho A) + \frac{\partial}{\partial s}(\rho V_s A) = 0 \quad (2.1)$$

$$\frac{\partial}{\partial t}(\rho V_s A) + \frac{\partial}{\partial s}[(\rho V_s^2 + P + \frac{B_\phi^2}{8\pi})A] = (P + \frac{\rho V_\phi^2}{2})\frac{dA}{ds} - \rho g_0 A \frac{dz}{ds} \quad (2.2)$$

$$\frac{\partial}{\partial t}(\rho V_\phi A^{\frac{3}{2}}) + \frac{\partial}{\partial s}[(\rho V_\phi V_s - \frac{B_\phi B_s}{4\pi}]A^{\frac{3}{2}}] = A \rho L_{trq} \quad (2.3)$$

$$\frac{\partial}{\partial t}(\sqrt{A} B_\phi) + \frac{\partial}{\partial s}[(B_\phi V_s - B_s V_\phi)\sqrt{A}] = 0 \quad (2.4)$$

$$\begin{aligned} \frac{\partial}{\partial t}[(\frac{\rho |\mathbf{V}|^2}{2} + \frac{P}{\gamma - 1} + \frac{|\mathbf{B}|^2}{8\pi})A] + \frac{\partial}{\partial s}\{[(\frac{\rho |\mathbf{V}|^2}{2} + \frac{\gamma P}{\gamma - 1} + \frac{B_\phi^2}{4\pi})V_s - \frac{B_s B_\phi V_\phi}{4\pi}]A\} \\ = -L_{rad}A - \rho V_s g_0 \frac{dz}{ds}A + \rho V_\phi \sqrt{A} L_{trq} \end{aligned} \quad (2.5)$$

as well as ideal gas equation of state

$$P = \frac{k_B}{m_h} \rho T. \quad (2.6)$$

There are three extra terms beside an ideal MHD model. The first one is gravity, in

Table 2.1: Meaning of each character in basic equations.

Character	Physical parameter
ρ	density
A	cross section area
t	time
s	distance along the field line
V_s	velocity along s direction
P	gas pressure
V_ϕ	velocity along ϕ direction
g_0	gravity
z	height
B_s	magnetic field along s direction
L_{trq}	transverse torque
B_ϕ	magnetic field along ϕ direction
\mathbf{V}	velocity vector
\mathbf{B}	magnetic field vector
L_{rad}	radiative loss
γ	ratio of specific heats, $\gamma = \frac{5}{3}$
T	temperature
m_h	mass of hydrogen atom, $m_h = 1.67 \times 10^{-24}$ g
k_B	Boltzmann constant, $k_B = 1.38 \times 10^{-16}$ erg K

our model, gravity g_0 is calculated by

$$g_0 = \frac{GM_{sun}}{(z + r_{sun})^2} \quad (2.7)$$

where G is gravitational constant, M_{sun} is the mass of the sun, r_{sun} is the radius of the sun.

The second extra term in our simulation beyond an ideal MHD model is the transverse torque L_{trq} . Alfvén wave is initialized by this transverse torque that mimics the convection motion at the photosphere. Following previous studies (e.g. Kudoh & Shibata, 1999; Matsumoto & Shibata, 2010), L_{trq} is modeled to have the following form

$$L_{trq} = r f_0(t) \left(\tanh\left(\frac{z - 0.75H_0}{0.075H_0}\right) - 1 \right) \quad (2.8)$$

where r is the radius of the cross section of the flux tube, H_0 is the scale height. $H_0 = 150$

km is used here. $f_0(t)$ determines the amplitude and time evolution of the artificial torque. We adjust the form and amplitude of the artificial torque by adjusting $f_0(t)$. In our study, L_{trq} has two forms, white noise or derived from observed transverse velocity spectra. We will describe in detail in the next chapter.

The third term is radiative loss L_{rad} which is the key term in our research. As discussed in section 1.2, radiative loss has a great effect on dynamics while at the same time difficult to treat. In this study, we follow the approximation approach by Carlsson & Leenaarts (2012). In this approach, the radiative loss is described by the following expression

$$L_{rad} = - \sum_{X_m} L_{X_m}(T) E_{X_m}(\tau) \frac{N_{X_m}(T)}{N_X} A_X N_H n_e \quad (2.9)$$

where the subscript X_m represents component of element X in ionization state m . X_m used in this approximation method are neutral hydrogen (H I), singly ionized calcium (Ca II) and singly ionized magnesium (Mg II) since they are the most important components for chromospheric radiative loss which have been discussed in section 1.2 (see Figure 1.3). T is temperature, A_X is the abundance of element X which is a constant for certain element and τ is optical depth, the definition of which is shown later. $L_{X_m}(T)$ and $\frac{N_{X_m}(T)}{N_X}$ are functions of temperature T , $E_{X_m}(\tau)$ is escape probability. They are given by fitting with a detailed radiative transfer calculation. N_H is the number density of hydrogen element and n_e is the number density of electrons. The aim of this approximation approach is to obtain a simple form of $L_{X_m}(T)$, $E_{X_m}(\tau)$ and $\frac{N_{X_m}(T)}{N_X}$ as a function of some physical parameters that we can calculate the radiative loss rate by submitting proper values into these functions without carrying out complete radiative transfer calculation.

$L_{X_m}(T)$ is the optical thin radiative loss function. It is expected to be a function of temperature. This is because in optical thin approximation, we could ignore the reabsorption of photons at first. We further assume that downward radiative de-excitation rate is larger than collisional de-excitation rate, which means that all the electrons leaving the ground state by collisional excitation will soon fall back to the ground state due to ra-

diative de-excitation, then the rate of photon emitted is only determined by collisional excitation from the ground state which is

$$L_{X_m} = \frac{N_{X_{m,1}}}{N_{X_m}} \sum_{j=2}^{n_1} \frac{\chi_{1j} C_{1j}}{n_e} \quad (2.10)$$

where $N_{x_{m,1}}$ represents number density of electrons on the ground level (level 1) of ionization state m of element X . n_1 is the highest energy level included in the calculation. It is impossible to contain unlimited numbers of energy levels. However, in practice, only a few levels are enough. χ_{1j} represents the energy difference between energy level j and the ground level, n_e is the number density of electrons. C_{1j} is the collisional coefficient that $N_{X_{m,1}} C_{1j}$ represents how many times of collisional excitation from the ground level to level j occurs in unit time, where C_{1j}/n_e is a function of temperature T (Rutten, 2003). $\frac{N_{X_{m,1}}}{N_{X_m}}$ is usually very close to 1, so that, if we ignore this little discrepancy, L_{X_m} could be treated as a function of only temperature T .

Practically, L_{X_m} is calculated by summation of all the energy released by radiative de-excitation in detailed radiative transfer calculation for certain ionization state. By fitting the relationship between temperature and L_{X_m} calculated by detailed radiative transfer from equation 2.10, the function $L_{X_m}(T)$ is obtained.

$E_{X_m}(\tau)$ is the escape probability which indicates the probability of a photon which could finally escape without being reabsorbed by the plasma on its propagation path. It is natural that this relation has a negative correlation with optical depth τ . The definition of optical depth is

$$\tau_\nu = \int_{x_1}^{x_2} \alpha_\nu dx \quad (2.11)$$

where x is spatial coordinate, ν is frequency and α is absorption coefficient. The optical depth needs to be defined between two points x_1 and x_2 on the route of the propagation of the light. Strictly speaking, one side of the integration should be the observer, while for most chromospheric lines, starting from some certain height h_0 (usually the base of the corona), due to the sudden decrease in density as well as other changes of the surrounding

environment, the absorption coefficient becomes so small that we can ignore it. (Take the example of Mg II lines, since the temperature in the corona is so high that most Mg ions are in a higher ionization level. As a result, the absorption coefficient for Mg II lines could be ignored). So that, when we refer to the optical depth at a certain height h , it is actually

$$\tau_\nu(h) = \int_h^{h_0} \alpha_\nu dx. \quad (2.12)$$

In practice, τ is not calculated, instead, since α usually have a positive relation with number density, it is assumed that τ also has a positive relation with column mass or column density. As a result, E_{X_m} is obtained by fitting the ratio of calculated radiative loss (equation 1.3) to calculated optically thin radiative loss (equation 2.10) as a function of column mass (for Mg II and Ca II) or column number density of neutral hydrogen (for hydrogen).

$\frac{N_{X_m}}{N_X}(T)$ indicates the ratio of number density of ions in specific ionization state m to the total number density of specific element X . Generally speaking, this ratio should be related with electron density, temperature, etc. as well as the previous state of the system. It is found from the detailed calculation that the fitting between ionization ratio and temperature yields a relatively satisfactory result (Carlsson & Leenaarts, 2012).

In this study radiative loss rate is obtained by substituting appropriate physical parameters into these functions by using equation 2.9. Electron density is calculated from the hydrogen ionization degree derived from the fitting. Currently, we limit the calculation range for radiative loss between 1.2 Mm and the transition region. The reasons are listed as follows: 1. radiative loss time scale below 1.2 Mm is much larger than dynamic time scale. We define radiative loss time scale to be the ratio of local dynamic energy density (estimated by $\frac{1}{2}\rho c_s^2$, c_s is sound speed which is assumed to be 10 km/s, ρ is density obtained from VALC model) to local radiative loss rate (from VALC model). Radiative loss time scale is around 300 s at 1.2 Mm and is expected to increase in a deeper region as the density increases drastically while radiative loss rate is maintained at the same order

and even decrease according to VALC model. The radiative loss time scale at 0.7 Mm is estimated to be around 10^4 s. On the other hand, It takes about only 50s for the sound wave to propagate from 0.7 Mm to 1.2 Mm if we assume the velocity of the sound wave is 10 km/s. As a result, radiative loss may have only minor effect on waves propagating in the lower chromosphere. 2. Technically it is difficult to obtain the ionization degree from fitting function at the low-temperature region (< 6000 K). 3. At the transition region, both radiative loss and heat flux conducted from the high temperature corona are important for energy balance. Since we do not include heat conduction in our calculation, it is reasonable to remove radiative loss in the transition region to compensate the missing of conduction flux.

2.3 Initial conditions

We assume a hydrostatic stratified atmosphere that

$$\frac{dP}{dz} = -\rho g_0 \quad (2.13)$$

as well as the equation of state of ideal gas (equation 2.6). Initial temperature distribution is a combination of VALC temperature model and a hyperbolic tangent distribution that is described below

$$T = \begin{cases} T_{\text{valc}}(z) & T \leq 1 \text{ Mm} \\ T_{\text{pho}} + \frac{1}{2}(T_{\text{cor}} - T_{\text{pho}})(\tanh(\frac{z-z_{\text{tr}}}{w_{\text{tr}}}) + 1) & T > 1 \text{ Mm} \end{cases} \quad (2.14)$$

where T_{cor} is the temperature of the corona that set to be 10^6 K, T_{pho} is the temperature of the photosphere set to be 6000 K, z_{tr} is the height of the transition region which is 2.25 Mm and w_{tr} relates with the width of transition region, which is set to be 0.05 Mm. Density at lower boundary is set to be 2.53×10^{-7} g cm $^{-3}$. After temperature is determined, pressure and density as a function of height is calculated by equation 2.13 and 2.14. The

distributions of temperature, gas pressure and density are shown in Figure 2.2 - 2.4. B_s at the photosphere is determined by gas pressure to maintain plasma beta around unity. As height increases, the distribution of B_s follows the assumption that

$$B_s A = \text{constant} \quad (2.15)$$

where A is the cross section area.

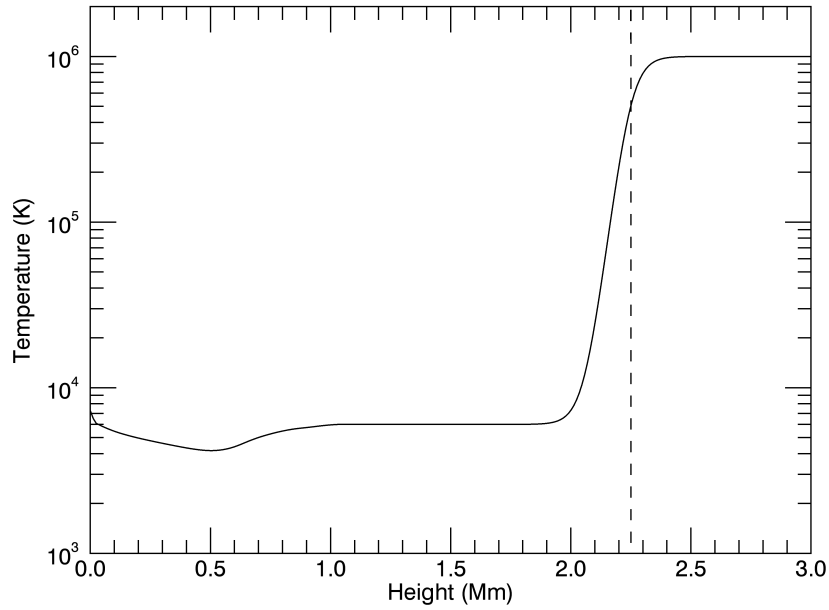


Figure 2.2: Initial temperature distribution as a function of height. Dashed line shows the height of the transition region, which is 2.25 Mm in this study.

2.4 Boundary conditions and numerical scheme

MHD equations are solved by the Modified Harten-Lax-van Lee approximate Riemann solver (HLLD; Miyoshi & Kusano, 2005), where "D" stands for Discontinuities. We set the scheme to be second order accuracy in space and time by applying the Monotonic Upwind Scheme for Conservation Laws (MUSCL) reconstruction with minmod slope limiter

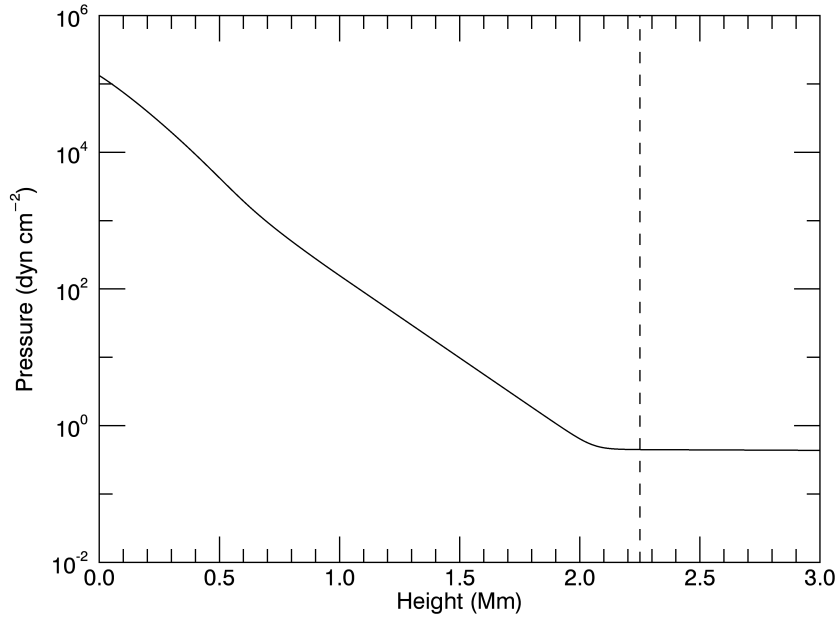


Figure 2.3: Initial pressure distribution as a function of height. Dashed line shows the height of the transition region, which is 2.25 Mm in this study

and the second order Total Variation Diminishing Runge-Kutta scheme (TVD RK2) on time evolution.

We have rigid wall boundary conditions at the lower boundary and free boundary condition at the top boundary. We include 2048 grid points and the spatial resolution is 10 km. Since the typical sound speed in the chromosphere is 10 km/s. The spatial resolution applied in our study can only resolve waves which have a period longer than 2 s. This is much shorter than typical wave period (around 10² s) in the chromosphere. As a result, our spatial discretization is enough to resolve waves in the chromosphere.

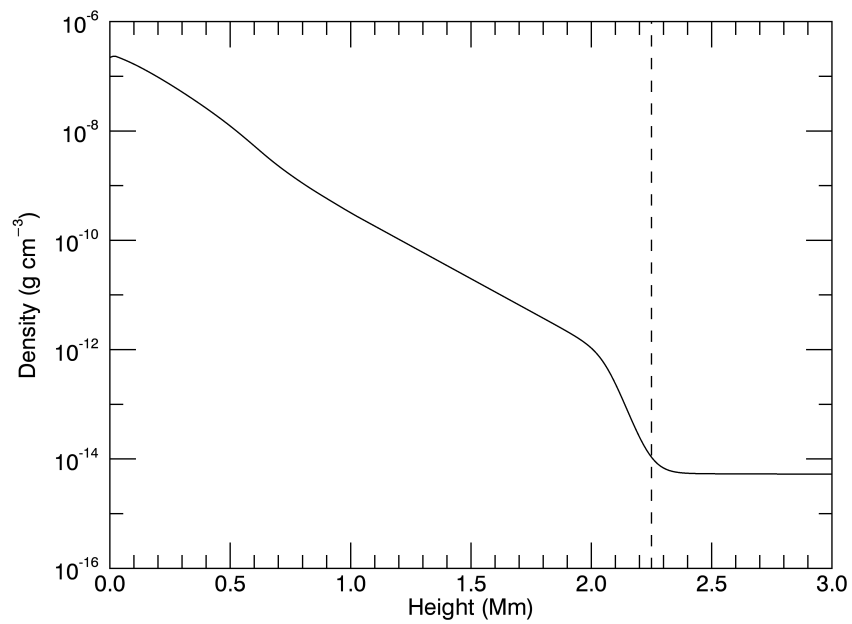


Figure 2.4: Initial density distribution as a function of height. Dashed line shows the height of the transition region, which is 2.25 Mm in this study.

Chapter 3

Results and analysis

3.1 Introduction

This chapter introduces the results of our calculation. We mainly concentrate on spicule height, radiative loss in the chromosphere and energy flux in the corona. In Section 3.2, comparison between the result with and without radiative loss of a sample case is shown to discuss the role of radiative loss. In Section 3.3, we show results of parameter survey for different input wave amplitude. In Section 3.4, we carry out parameter survey on flux expansion. In this section, we include realistic input wave power spectrum and compare our results to realistic reference values of the sun. In Section 3.5 we briefly discuss the effect of input wave spectra and the photosphere magnetic fields.

3.2 Role of radiative loss

In this section, we compare the result with and without radiative loss for a typical case. Basic settings are described in the last chapter while we mention that the expansion of flux tube and wave driving source vary case by case. In this section, the geometry setting of the flux tube, which is the radius of flux tube as a function of height is shown in Figure 2.1. The ratio of the radius of the flux tube in the corona to radius in the photosphere is

13.5.

We carry out two calculations. The calculations last 1600 seconds which is around 8 times of sound wave transverse time (the time of sound wave propagating from the bottom of the photosphere to the transition region). All the settings except radiative loss are the same between the two calculations. In the first calculation we remove radiative loss which we call case N while the second includes radiative loss that is called case R. In case R, radiative loss is included after 200 s and linearly increases from 0 to normal value within 100 s by the following way

$$L_{rad}(t) = L_{rad_0} \frac{t - 200s}{100s} \quad (200s < t < 300s) \quad (3.1)$$

where L_{rad} is radiative loss used in the simulation and L_{rad_0} is radiative loss calculated by equation 2.9.

We expect the initial transverse velocity to be white noise signal. which requires a frequency range. In our case, we limit the maximum frequency f_{max} to be 0.1 Hz and minimum frequency f_{min} to be 6.25×10^{-4} Hz, which is the total calculation time. The initial transverse velocity has the form.

$$V_{\phi}(t) = \sum_i C_i \sin(2\pi f_i t + \phi_i) \quad (3.2)$$

where C_i is the amplitude of frequency f_i . In white noise case, C_i is a constant for different i . Frequency f_i is chosen to be 10000 points averagely distributed between f_{min} and f_{max} . ϕ_i are phases which are random numbers between 0 and 2π for each i . To obtain this white noise signal, we set the intensity of torque to be the acceleration that has the form

$$L_{trq} \propto \frac{dV_{\phi}}{dt} = \sum_i 2\pi f_i C_i \cos(2\pi f_i t + \phi_i). \quad (3.3)$$

In this calculation, the root mean square of transverse velocity at the lower boundary

is around 1.27 km/s in this section. We will show the result of the parameter survey on the root mean square of transverse velocity in Section 3.3. The power spectrum of transverse velocity at the bottom for case N is shown in Figure 3.1.

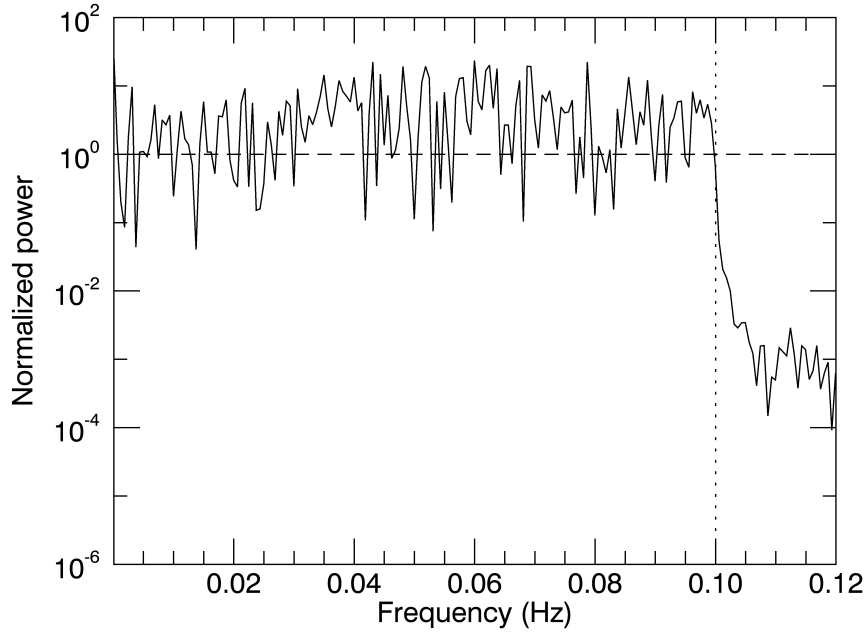


Figure 3.1: Power spectrum of the transverse velocity at the bottom for case N. Power is normalized by averaged value (dashed line). Dotted line shows the cut frequency which is 0.1 Hz.

We compare results between calculations with and without radiative loss. Figure 3.2 shows time slice of the spatial distribution of density. Figure 3.3 shows the integration of energy flux in the corona, where the height of the corona is chosen to be 10 Mm.

From Figure 3.2, referring to spicule height, the effect of radiative loss is rather obvious. In case N, spicule height increases with time since energy is input continuously into the system. From the energy conversion perspective, there is no energy loss in the atmosphere and nearly all the energy input, except the part of energy that goes into the corona, will convert to internal energy and gravitational energy which is reflected by the height of spicule. As a result, it is expected that the height of spicules become higher and higher as time evolves. On the other hand, in case R, the height of spicule is greatly

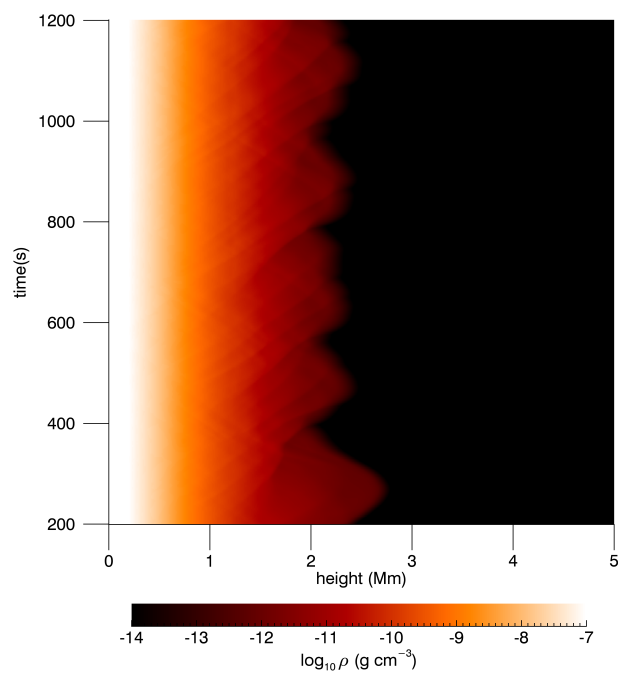
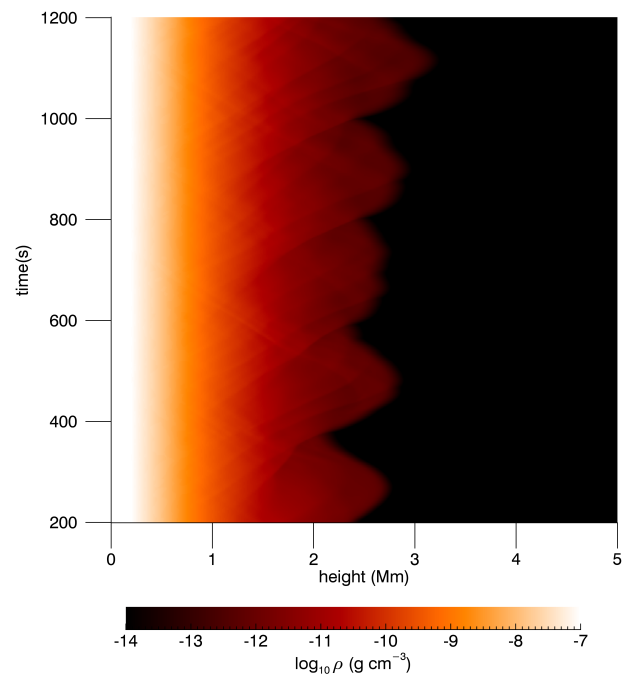


Figure 3.2: Time slice of the distribution of density. Upper: without radiative loss (case N). Lower: with radiative loss (case R). Radiative loss is switched off before 200s which makes the first peak stronger in case R.

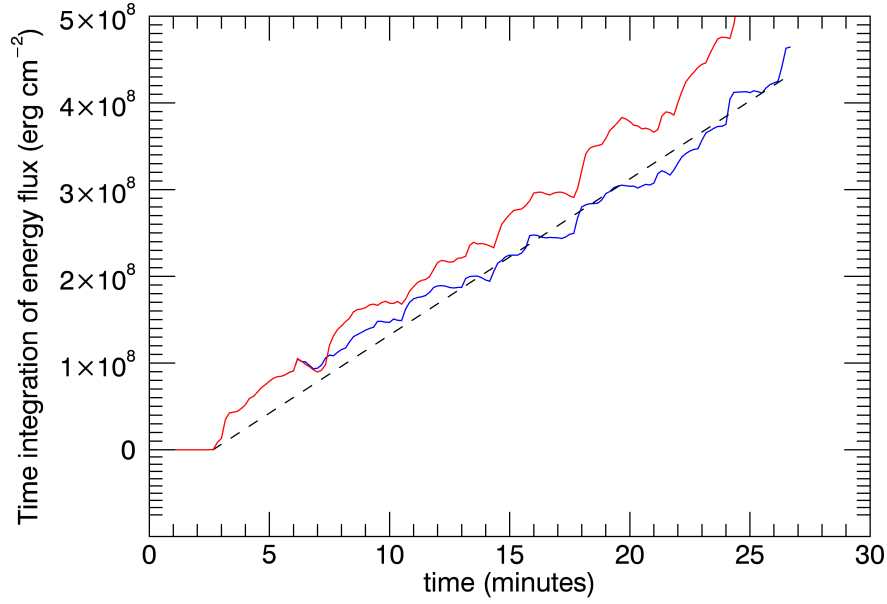


Figure 3.3: Time integration of energy flux as a function of time. Red line for case N and blue line for case R. Dashed line shows the reference flux required for corona heating which is $3 \times 10^5 \text{ erg cm}^{-2}\text{s}^{-1}$ (Withbroe & Noyes, 1977).

suppressed because part of the energy, which is going to increase the height of spicules in case N, is lost by radiation in case R.

Figure 3.3 shows that the time averaged energy flux in the corona is $4.0 \times 10^5 \text{ erg cm}^{-2}\text{s}^{-1}$ for case N while $3.2 \times 10^5 \text{ erg cm}^{-2}\text{s}^{-1}$ for case R. The energy flux for case R is around 80% of the energy flux in case N. This result shows that radiative loss does not affect energy flux in the corona obviously. It is considered that energy flux in the corona is dominated by Alfvén wave (Kudoh & Shibata, 1999). Incompressible nature of Alfvén wave makes it insensitive to radiative loss. Alfvén wave does not change local temperature and density which are crucial parameters for radiative loss, thus it is reasonable that the energy flux in the coronal is not affected greatly by radiative loss.

3.3 Relation between initial wave amplitude and energy flux in the corona

In this section, we are going to discuss the effect of input transverse wave amplitude and whether the role of radiation changes with different wave amplitudes. The geometry setting of the flux tube is the same as Section 3.2 and shown in Figure 2.1. The transverse torque still mimics the white noise transverse velocity but a multiplier is applied on the initial transverse torque to create different amplitudes. Figure 3.4 shows the relation between root mean square of initial transverse wave amplitude and energy flux in the corona. When the initial amplitude of transverse velocity is larger, the nonlinearity of the Alfvén wave also becomes stronger. As a result, acoustic wave initialized by mode conversion becomes stronger. Since only acoustic wave is affected by radiative loss noticeably, the total energy flux is easier to be affected by radiative loss only when the initial amplitude is large. Figure 3.5 shows the same plot but in log scale. The WKB approximation gives the flux in the corona F to be proportional to the square of initial transverse velocity which is shown by the dash-dotted lines that have slopes of 2. It is shown that, when the initial transverse velocity is larger than 1 km/s, the nonlinearity effect starts to take effect that both the red and blue lines (indicate results with or without radiation) begin to deviate from the dash-dotted line.

3.4 Effect of flux tube expanding

In this section, we try to apply realistic transverse spectrum that matches the observed transverse spectrum on the sun. We compare the energy flux in the corona, radiative loss in the chromosphere between our simulation results and realistic values. These comparisons are done along with the parameter survey on the degree of expansion of the flux tube

We adjust the initial torque by the same method described in Section 3.2 that the spectrum of the initial transverse velocity is consistent with the observed one by Matsumoto

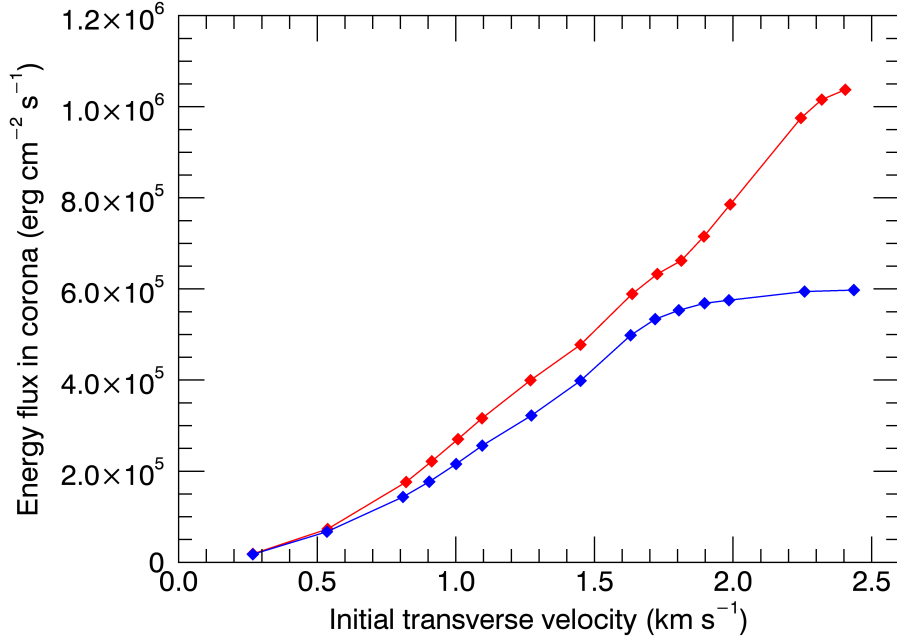


Figure 3.4: Time averaged energy flux as a function of root mean square of initial transverse wave amplitude. Red lines shows results without radiative loss. Blue line shows results with radiative loss.

& Shibata (2010), which is shown in Figure 3.6. This time we adjust the multiplier that the root mean square of transverse velocity is expected to have an amplitude of around 1 km/s. Which is the typical transverse velocity amplitude on the sun (Kudoh & Shibata, 1999; Matsumoto & Shibata, 2010). In this analysis, we also pay attention to the height of spicules. Cases with spicule launching are marked by red points, which is defined that the maximum height of the transition region during the simulation could reach at least 2 times of the initial height of the transition region.

We adjust the shape of flux tubes in different expanding degree. The expanding factor ϵ is defined as

$$\epsilon = \frac{r_c}{r_0} \quad (3.4)$$

where r_0 is radius of flux tube at the photosphere ($z = 0$ Mm). r_c is radius of flux tube at the corona ($z = 10$ Mm). Flux tubes with different expanding factors used in this section are displayed by solid lines and dotted lines in Figure 3.7

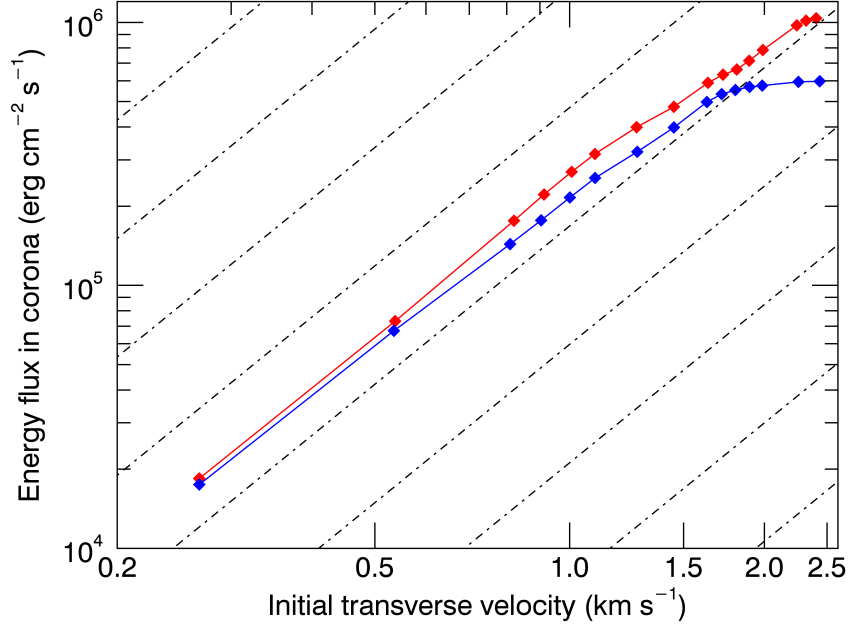


Figure 3.5: The same plot as Figure 3.4 in log scale. Dash-dotted lines have slopes of 2 which show the result of WKB approximation that the energy flux in the corona $F \propto v_\phi^2$

Our radiative MHD simulation can also obtain radiative loss on each point of the expanding flux tube. Total radiative loss rate per unit area R_{loss} is calculated by

$$R_{loss} = \int L_{rad,eff} ds \quad (3.5)$$

where

$$L_{rad,eff} = L_{rad}A(s)/A_c \quad (3.6)$$

$A(s)$ is cross section area as a function of s , which is the spatial coordinate on the direction of field line. A_c is cross section area at the corona ($z = 10$ Mm). $L_{rad,eff}$ is the effective radiative loss rate with a compensation of expanding effect. On the other word, instead of only mattering inside the expanding flux tube, the effective radiative loss is an effective value of radiative loss to cover the whole cylinder which has a constant cross section of A_c . We need to note again that our radiative loss rate L_{rad} here can only describe radiative loss in the middle and higher chromosphere (see Section 2.2).

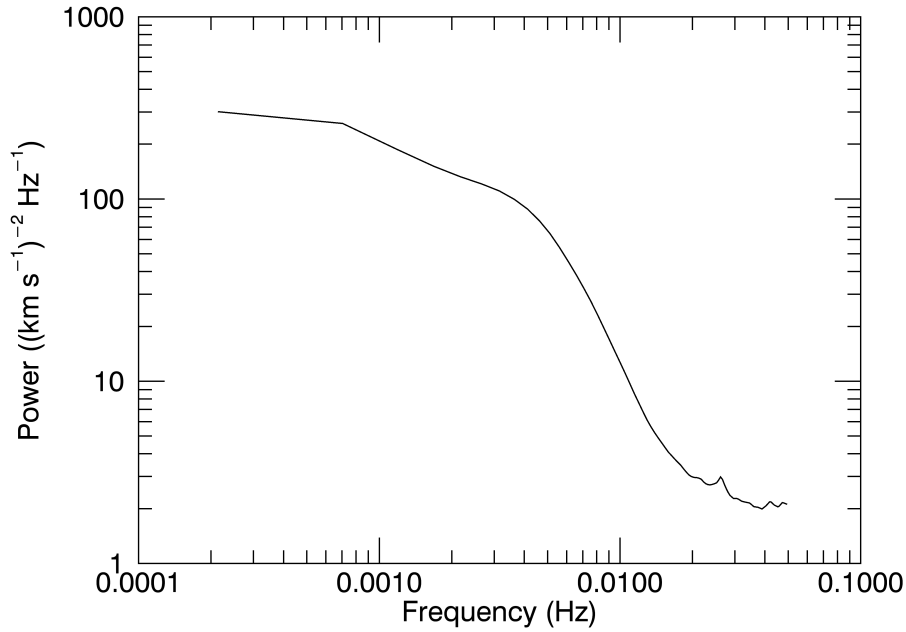


Figure 3.6: Observed power spectrum of photospheric horizontal velocity, modified from Figure 2 in Matsumoto & Shibata (2010).

From Figure 3.8 we learn that generally the energy flux is larger enough for corona heating. While we find that the energy flux decreases as the flux tube expands because energy flux is defined in per unit area. On the other hand, the energy flux also decreases when the flux tube has a smaller expanding factor. This is because a flux tube with smaller expanding factor has stronger background magnetic field intensity thus higher Alfvén speed, which leads to a longer wavelength of Alfvén wave and higher reflection rate at the transition region.

From Figure 3.9, the radiative loss (per unit area) in the range where expanding factor is more than 12 decreases with expanding factor increasing. In the range where expanding factor is less than 12, the behavior is a little strange, It could be caused by the competition between less nonlinearity which produces less acoustic wave thus less radiation and less expanding tube that energy in unit area becomes larger. One needs to note that in each case, we are only measuring the area that could be covered by expanding flux tube. If the expanding factor is too small, such flux tube is unrealistically thin that can only cover

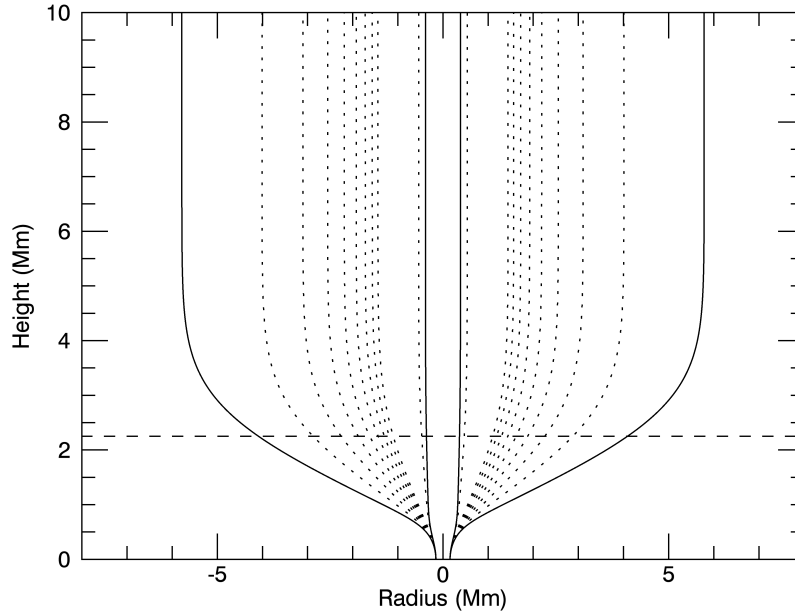


Figure 3.7: Shape of flux tubes in different cases. Solid lines show the maximum and minimum expansion of flux tubes. Dotted lines show the intermediate cases. Dashed line represents the height of the transition region which is 2.25 Mm.

a tiny part of the solar surface. It also worth noticing that when the expanding factor is between 10 and 15, this model is consistent with a whole scenario of chromospheric heating, spicule launching as well as providing enough energy flux for coronal heating.

3.5 Effect of input wave spectrum and the photosphere magnetic field

Other parameters that are likely to affect wave flux in the corona (defined as at $z = 10$ Mm, where z is height) and chromospheric heating include input transverse velocity spectrum and magnetic field intensity. We note that in Section 3.3 and 3.4, where we include two different types of input transverse waves, i.e. white noise and realistic power spectrum. We find that even with the same root mean square of input wave amplitude, the energy flux in the corona is much larger in the latter case. For higher frequency

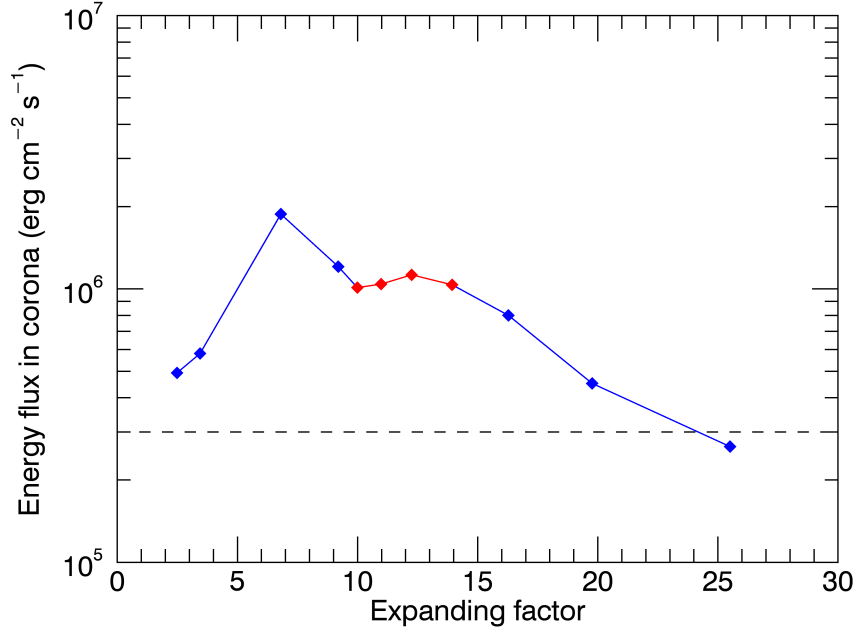


Figure 3.8: Time averaged energy flux as a function of expanding factor measured at $z = 10$ Mm. Dashed line shows the reference value required for the corona heating which is $3 \times 10^5 \text{ erg cm}^{-2} \text{ s}^{-1}$ (Withbroe & Noyes, 1977). Cases with successful spicule launching are marked by red points and red lines.

transverse waves, they produce higher frequency acoustic waves by mode conversion, which is easier to steepen and to be dissipated. As a result, a larger amount of wave energy is dissipated in the lower chromosphere. Parameter survey done by Matsumoto & Shibata (2010) shows that waves which has a period shorter than 60 s (frequency higher than 0.017 Hz) are not efficient to transport energy to the corona. In the white-noise case, we include transverse wave that has energy distributed equally in the frequency range between 0.0625 Hz and 0.1 Hz while for the realistic-input case, the power of transverse velocity at lower boundary mainly lies in the range smaller than 0.02 Hz. This discrepancy causes the difference of the energy flux in the corona.

For the effect of magnetic field, we can imagine that stronger magnetic field gives smaller nonlinearity of Alfvén wave that we may expect larger energy flux in the corona. In this simulation, we chose the same setting as case R in Section 3.2 except that the magnetic field at the photosphere B_{pho} is adjusted that plasma beta at lower boundary

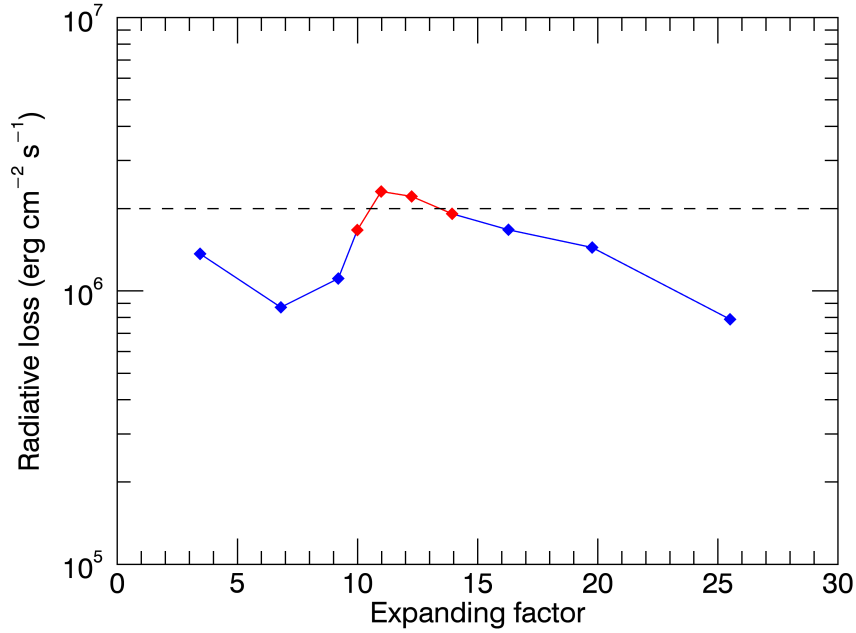


Figure 3.9: Radiative loss rate (per unit area) as a function of expanding factor. Dashed line shows the reference value required for chromospheric heating in the middle and higher chromosphere which is $2 \times 10^6 \text{ erg cm}^{-2}\text{s}^{-1}$ (Withbroe & Noyes, 1977). Cases with successful spicule launching are marked by red points.

is set to be 1.2 and 0.8 respectively. Our calculation shows that the energy flux in the corona becomes $2.4 \text{ erg cm}^{-2}\text{s}^{-1}$ and $4.2 \text{ erg cm}^{-2}\text{s}^{-1}$ for plasma beta equals 1.2 and 0.8, respectively. The time integration of energy flux in the corona is shown in Figure 3.10. In terms of radiative loss, total radiative loss in the middle and higher chromosphere becomes $2.63 \times 10^5 \text{ erg cm}^{-2}\text{s}^{-1}$ and $2.24 \times 10^5 \text{ erg cm}^{-2}\text{s}^{-1}$, respectively. This result shows that for 20% difference in plasma beta at bottom of the photosphere, change of energy flux and radiative loss are around 10 – 30% .

From Figure 3.3 we learn that our simulation could provide enough energy flux in the corona, which is more than three times of the required value. From the analysis in this section, it seems that energy flux is still enough for coronal heating even the photospheric magnetic field of network region becomes weaker (on the order of 10%). On the other hand, since chromospheric radiative loss only reaches the lowest level (Figure 3.9) of the required value, there is a possibility of chromospheric radiative loss being insufficient if

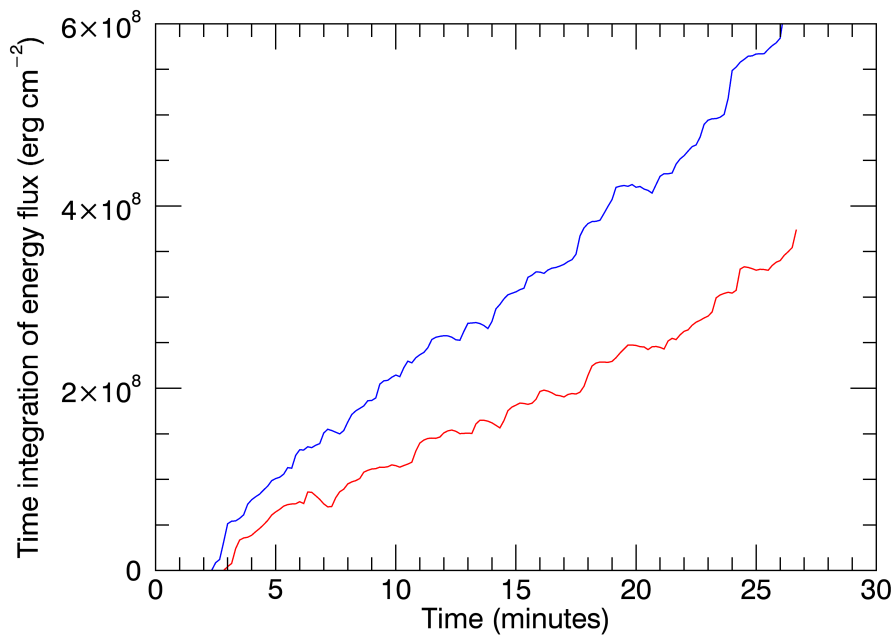


Figure 3.10: Time integration of energy flux as a function of time. Red line and blue line show the case that plasma beta at bottom is 1.2 and 0.8, respectively. The flux in the corona for lower bottom plasma beta case is larger.

the magnetic field at the bottom becomes stronger.

Chapter 4

Discussion

4.1 Spatial distribution of radiative loss

We chose the expanding factor $\epsilon = 12.25$ case in Section 3.3. This case is one of the four good examples that atmosphere heating and spicule launching could be obtained simultaneously. We calculate time averaged effective radiative loss by the same method from equation 3.6 but as a function of column mass. The result is shown in Figure 4.1, with radiative loss from VALC model is shown in dashed line. Here the purpose of using column mass instead of height is to avoid the uncertainty of the transition region height due to spicule launching. We find that the spatial distribution of radiative loss from VALC model is similar to the time averaged profile, especially in the middle and higher chromosphere when column mass is smaller than 10^{-4}g cm^{-2} , which is around 1.4 Mm in VALC model. This is not surprising because even though VALC model itself assumes time-independent static conditions, it is based on spectral observations of the solar atmosphere, which is actually a dynamic one. As a result, we may expect the VALC model to represent time average of the solar dynamic atmosphere.

This consistency between VALC and radiative loss in our simulation further validate the feasibility of the Alfvén wave driven model. We also note that radiative loss in our simulation is smaller than VALC model in the lower chromosphere. This may indicate

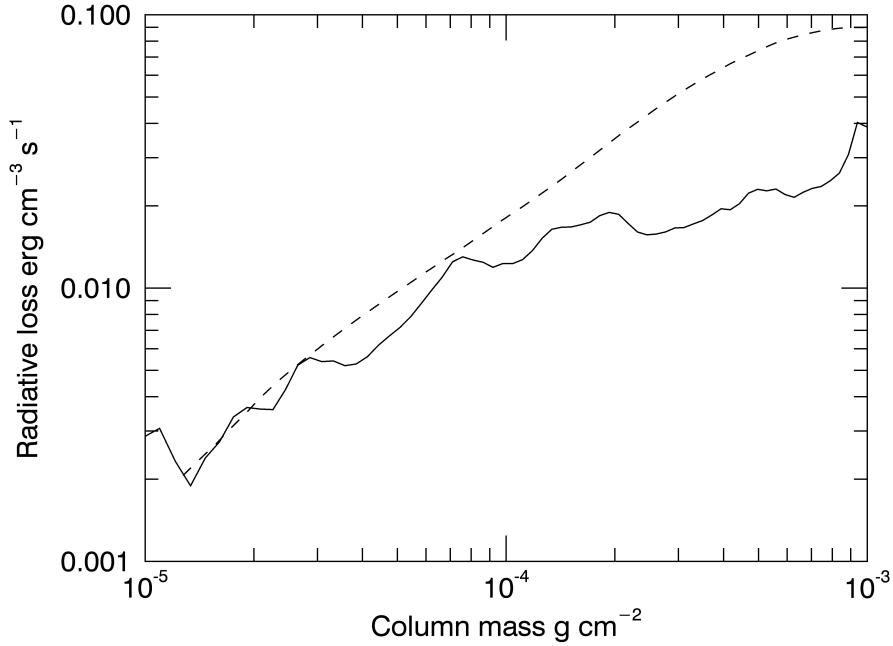


Figure 4.1: Spatial distribution of radiative loss as a function of column mass. Solid line shows the effective radiative loss in our simulation. Dashed line shows the radiative loss of VALC model.

the lack of energy source in the lower chromosphere that is consistent with the discussion in Section 3.5.

4.2 Estimation of the expanding factor

In Section 3.3, we conclude that if the expanding factor is around 10 – 15, the Alfvén wave driven model is appropriate to explain a whole scenario of chromospheric heating, spicule launching as well as provide enough energy flux for coronal heating. Then we discuss whether expanding factor 10 – 15 is an appropriate value from observational standpoints.

From Section 3.3, The relation between expanding factor ϵ and magnetic field or cross section area is

$$\epsilon^2 = \frac{B_{x_0}}{B_c} = \frac{A_c}{A_{x_0}} \quad (4.1)$$

where B_{x_0} , B_c , A_{x_0} and A_c are magnetic fields at the the lower boundary, magnetic field at the corona, cross section area at the lower boundary and cross section area at the corona, respectively. The intensity of magnetic field decreases from a typical value of 1000 G in the network regions down to 2 – 6 G (Long et al., 2013) in the corona. Consequently, the ratio between photospheric magnetic field and coronal magnetic field is 167 – 500, which leads to an effective expanding factor around 13 – 22. Our expanding factor of 10 – 15 is a reasonable one.

4.3 Comparison with previous researches

There are other observational works focusing on waves in the solar atmosphere (e.g. De Pontieu et al., 2007b; Kanoh et al., 2016). In the observation carried out by De Pontieu et al. (2007b), the swing motions of spicules are interpreted as Alfvénic waves which are responsible for transporting energy to the corona. Their observation shows that most spicules have maximum transverse velocities of about 10 to 30 km/s with a peak of 15 km/s in the velocity distribution. In our simulation, if we consider the same case of that used in Section 4.1, we obtain the root mean square of transverse velocity in higher chromosphere (at $z = 2.1$ Mm) to be 15 km/s which corresponds to a velocity amplitude of 21 km/s that is larger than that observed in De Pontieu et al. (2007b) but still in the reasonable range.

Our study is an extension of the studies of Kudoh & Shibata (1999) and Matsumoto & Shibata (2010). The main difference between Section 3.3 in our study and Kudoh & Shibata (1999) is that we include radiative loss. Comparing the blue line in Figure 3.4 and Figure 18 in Kudoh & Shibata (1999) we find that we require a larger initial velocity to obtain the same level of energy flux in the corona. This difference is mainly caused by spectrum of input transverse wave that discussed in Section 3.5.

The main difference between Section 4.2 and Matsumoto & Shibata (2010) is that we include more realistic approximation of radiative loss approach introduced by Carlsson & Leenaarts (2012). The main advantage of our study is that we can obtain the realistic radiative loss which is spatially consistent with VALC model (Section 4.1). The radiative loss term used by Matsumoto & Shibata (2010) is a constant cooling time model introduced by Anderson & Athay (1989) which is derived from the cooling profile of VALC model while we can reproduce the VALC radiative loss profile from a different approach (Figure 4.1). Another difference is that we use a different initial temperature distribution. The expanding factor of flux tube in Matsumoto & Shibata (2010) is around 13. If we compare the energy flux between their simulation (Figure 8 in Matsumoto & Shibata (2010)) and ours (Figure 3.8, choosing the point where the expanding factor is around 13). The energy flux in our simulation is around twice of that in Matsumoto & Shibata (2010). we conclude that this difference is caused by temperature distribution in the chromosphere. Both of the two studies use gravity stratified static atmosphere as the initial condition. However, in Matsumoto & Shibata (2010), the chromosphere has an almost constant temperature of 5000 K. Generally speaking the temperature in the chromosphere in our simulation is higher than that in Matsumoto & Shibata (2010). which causes a larger scale height that the density decrease in our simulation is slower than that of Matsumoto & Shibata (2010), which further lead to a smaller Alfvén speed in our simulation (Figure 4.2). As a result, the wavelength of Alfvén wave in our simulation is shorter that Alfvén wave is easier to penetrate into the corona, which leads to a larger energy flux in our simulation. If we use the same initial temperature distribution as that used in Matsumoto & Shibata (2010) in our simulation, the energy flux in the corona is $4.64 \times 10^5 \text{ erg cm}^{-2}\text{s}^{-1}$ which is comparable to the result of Matsumoto & Shibata (2010) (see the white circles in Figure 8 of Matsumoto & Shibata (2010)). However, the radiative loss is not enough. Using equation 3.5, averaged radiative loss is only $1.53 \times 10^6 \text{ erg cm}^{-2}\text{s}^{-1}$, which is insufficient for chromospheric heating, due to the low temperature.

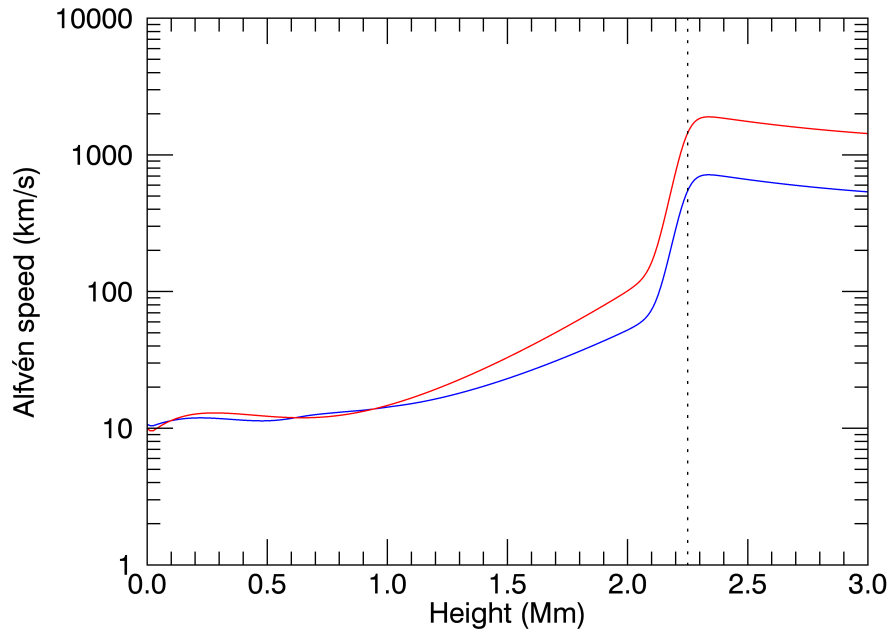


Figure 4.2: Distribution of background Alfvén speed as a function of height. Red line: when use the temperature distribution of Matsumoto & Shibata (2010). Blue line: when use the temperature distribution used in our simulation (equation 2.14). Dotted line shows the height of the transition region which is 2.25 Mm

Simulations of Brady & Arber (2016) give the chromosphere cooling rate that is spatially consistent with VAL models. This result is similar to ours but the radiative loss is treated more crudely comparing with our simulation. Our simulation has the advantage that the radiative loss treatment considers the realistic atomic models. On the other hand, in Brady & Arber (2016), they assume that the radiative loss is balanced by shock heating and carry out two simulations with the same initial conditions. The radiative loss is added in the second simulation to be the time averaged value of the shock heating rate in the first simulation. The consistency of radiative loss rate among our simulation, Brady & Arber (2016) and VAL models further emphasize the significant role of shock wave dissipation in chromospheric heating.

Chapter 5

Summary and Future Prospects

The solar atmosphere heating problem, which contains chromospheric and coronal heating problem, is still one of the most charming and challenging problems in solar physics. Our current understanding is unprecedented while there are still lots of problems left to be solved. The biggest problem is that the heating mechanism of both the chromosphere and the corona is still unclear. Though previous theoretical studies could give many constraints, there are many assumptions need to be set, one of which is the treating of radiative loss. Previous models usually ignore radiative loss or treat it crudely due to its difficulty while radiative loss is a dominant term in chromospheric energy loss. This study aims to investigate the effect of radiative loss on waves in the chromosphere as well as give a trial on a relatively simple atmosphere model that could explain chromospheric heating, spicule launching as well as enough energy transportation to the corona simultaneously. Our study focuses on an expanding flux tube which mimics the atmosphere above a magnetic concentration area such as the network regions, we solve the 1.5D ideal MHD equations by HLLD scheme with approximated radiative loss model.

We found that radiative loss have a minor effect on energy flux in the corona, except in the situation that the initial transverse wave is very large, while greatly affects the height of spicules. Our parameter survey suggests that Alfvén wave driven model could explain chromospheric heating and spicule launching simultaneously, as well as transport enough

energy to the corona which is responsible for coronal heating. The time averaged radiative loss in middle and the higher chromosphere is consistent with VALC model in terms of spatial distribution.

The future work of this study includes extending the parameter ranges to carry out parameter survey on magnetic field intensity and initial temperature distribution, in order to obtain a deeper understanding of the role of radiative loss in various conditions. Then we plan to extend the study to multi-dimension. The role of magnetic fields becomes more complicated and interesting. For example the presence of type-II spicules, which are more dynamic. Their formation is closely related with 3D geometry (Martínez-Sykora et al., 2011, 2017). Another aspect of the necessity of multi-dimensional study is on spectral synthesizing. Since chromosphere lines are usually affected by NLTE and optical depth effects which make a direct connection from observed line profile to physical condition extremely difficult that a forward modeling in combination of synthesizing is usually a powerful tool in interpreting observation. It is known that many chromosphere line profiles, especially line centers, are easily affected by the 3D structure of the atmosphere, among them include $H\alpha$, Mg II h&k, Ca II H&K which are important diagnostic lines in the chromosphere (Sukhorukov & Leenaarts, 2017). As a result, our model's extending to 3D is expected to be very helpful for data analysis for the next generation solar observatories, including Solar-C. One of the scientific goals of the Solar-C satellite is to reveal how much of wave dissipation contributes to the chromospheric and coronal heatings (Suematsu & Solar-C Working Group, 2016).

Acknowledgments

Deepest gratitude to my supervisor Dr. Yokoyama, T. for his careful instruction and kindly encouragement during the two years of my master course. Not only his depth of knowledge but also his sense of responsibility show me the direction of how to step closer to a respectful researcher and educator.

Many thanks to all the laboratory members. Iijima, H., Kaneko, T., Wang, S., Kono, S., Shoda, M., Oi, Y., Ichimura, C., Bekki, Y., and Mineta, R. Thanks for your discussions, advices, comments and sometimes funny jokes. It is my honor to join this laboratory. Because of you, every second here is so enjoyable. Wish you all the best for your future.

Special thanks to Dr. Rutten, R., Dr. Watanabe, T. and Dr. Shimizu, T. for their lectures and discussions on MHD and radiation, which are the two main parts of this study.

Thanks to all my friends, no matter you are close to me or far away. your support is always my powerful motivator. Hope you will be happy every day.

At last, Thanks to my parents, for giving me the chance to experience this amazing world, for everything you did for me. I am so lucky to be your child.

References

- Anderson, L. S., & Athay, R. G. 1989, *ApJ*, 336, 1089
- Arber, T. D., Brady, C. S., & Shelyag, S. 2016, *ApJ*, 817, 94
- Bello González, N., et al. 2010, *ApJL*, 723, L134
- Brady, C. S., & Arber, T. D. 2016, *ApJ*, 829, 80
- Carlsson, M., & Leenaarts, J. 2012, *A&A*, 539, A39
- Cavallini, F. 2006, *SoPh*, 236, 415
- De Pontieu, B., et al. 2007a, *PASJ*, 59, S655
- . 2007b, *Science*, 318, 1574
- . 2014, *SoPh*, 289, 2733
- Deng, Y., Liu, Z., & CGST Group. 2012, in *Astronomical Society of the Pacific Conference Series*, Vol. 463, Second ATST-EAST Meeting: Magnetic Fields from the Photosphere to the Corona., ed. T. R. Rimmele, A. Tritschler, F. Wöger, M. Collados Vera, H. Socas-Navarro, R. Schlichenmaier, M. Carlsson, T. Berger, A. Cadavid, P. R. Gilbert, P. R. Goode, & M. Knölker, 405
- Fossum, A., & Carlsson, M. 2005, *Nature*, 435, 919
- Gudiksen, B. V., Carlsson, M., Hansteen, V. H., Hayek, W., Leenaarts, J., & Martínez-Sykora, J. 2011, *A&A*, 531, A154

- Guerreiro, N., Carlsson, M., & Hansteen, V. 2013, *ApJ*, 766, 128
- Hollweg, J. V., Jackson, S., & Galloway, D. 1982, *SoPh*, 75, 35
- Iijima, H. 2016, PhD thesis, Department of Earth and Planetary Science, School of Science, The University of Tokyo, Japan
- Jess, D. B., Morton, R. J., Verth, G., Fedun, V., Grant, S. D. T., & Giagkiozis, I. 2015, *SSRev*, 190, 103
- Kanoh, R., Shimizu, T., & Imada, S. 2016, *ApJ*, 831, 24
- Kosugi, T., et al. 2007, *SoPh*, 243, 3
- Kudoh, T., & Shibata, K. 1999, *ApJ*, 514, 493
- Langanen, Ø., De Pontieu, B., Carlsson, M., Hansteen, V. H., Cauzzi, G., & Reardon, K. 2008, *ApJL*, 679, L167
- Lemen, J. R., et al. 2012, *SoPh*, 275, 17
- Liu, Z., et al. 2014, *Research in Astronomy and Astrophysics*, 14, 705
- Long, D. M., Williams, D. R., Régnier, S., & Harra, L. K. 2013, *SoPh*, 288, 567
- Martínez Pillet, V., et al. 2011, *SoPh*, 268, 57
- Martínez-Sykora, J., de Pontieu, B., Hansteen, V., Rouppe van der Voort, L., Carlsson, M., & Pereira, T. M. D. 2017, *Science*, 356, 1269
- Martínez-Sykora, J., Hansteen, V., & Moreno-Insertis, F. 2011, *ApJ*, 736, 9
- Matsumoto, T., & Shibata, K. 2010, *ApJ*, 710, 1857
- Matthews, S. A., Collados, M., Mathioudakis, M., & Erdelyi, R. 2016, in *procspie*, Vol. 9908, Ground-based and Airborne Instrumentation for Astronomy VI, 990809

- Miyoshi, T., & Kusano, K. 2005, *Journal of Computational Physics*, 208, 315
- Pesnell, W. D., Thompson, B. J., & Chamberlin, P. C. 2012, *SoPh*, 275, 3
- Rutten, R. J. 2003, *Radiative Transfer in Stellar Atmospheres*
- Scharmer, G. B., Bjelksjo, K., Korhonen, T. K., Lindberg, B., & Petterson, B. 2003, in *Proc. SPIE, Vol. 4853, Innovative Telescopes and Instrumentation for Solar Astrophysics*, ed. S. L. Keil & S. V. Avakyan, 341–350
- Scherrer, P. H., et al. 2012, *SoPh*, 275, 207
- Shimojo, M., et al. 2017, *SoPh*, 292, 87
- Skogsrud, H., Rouppe van der Voort, L., De Pontieu, B., & Pereira, T. M. D. 2015, *ApJ*, 806, 170
- Sobotka, M., Heinzl, P., Švanda, M., Jurčák, J., del Moro, D., & Berrilli, F. 2016, *ApJ*, 826, 49
- Sterling, A. C. 2000, *SoPh*, 196, 79
- Sterling, A. C., Shibata, K., & Mariska, J. T. 1993, *ApJ*, 407, 778
- Suematsu, Y., Shibata, K., Neshikawa, T., & Kitai, R. 1982, *SoPh*, 75, 99
- Suematsu, Y., & Solar-C Working Group. 2016, in *Astronomical Society of the Pacific Conference Series, Vol. 504, Coimbra Solar Physics Meeting: Ground-based Solar Observations in the Space Instrumentation Era*, ed. I. Dorotovic, C. E. Fischer, & M. Temmer, 299
- Sukhorukov, A. V., & Leenaarts, J. 2017, *A&A*, 597, A46
- Tian, H., et al. 2014a, *ApJ*, 786, 137
- . 2014b, *Science*, 346, 1255711

- Tritschler, A., et al. 2015, in Cambridge Workshop on Cool Stars, Stellar Systems, and the Sun, Vol. 18, 18th Cambridge Workshop on Cool Stars, Stellar Systems, and the Sun, ed. G. T. van Belle & H. C. Harris, 933–944
- Tsiropoula, G., Tziotziou, K., Kontogiannis, I., Madjarska, M. S., Doyle, J. G., & Suematsu, Y. 2012, *Space Sci. Rev.*, 169, 181
- Tsuneta, S., et al. 2008, *SoPh*, 249, 167
- Vernazza, J. E., Avrett, E. H., & Loeser, R. 1981, *ApJS*, 45, 635
- Wedemeyer-Böhm, S., Lagg, A., & Nordlund, Å. 2009, *Space Sci. Rev.*, 144, 317
- Withbroe, G. L., & Noyes, R. W. 1977, *ARA&A*, 15, 363